Transient Stability Analysis and Control Strategy for Paralleled Grid-forming Renewable Power Generations under Symmetric Faults

Sen Huang, Jun Yao, *Member*, *IEEE*, Wenwen He, Dong Yang, and Hai Xie

***Abstract*—Similar to synchronous generators (SGs), symmetrical short-circuit faults can reduce the stability margin of grid-forming renewable power generation (GFM-RPG), thereby heightening the risk of transient instability. While existing studies primarily examine single-machine infinite-bus systems, this work explores transient stability challenges inherent in paralleled GFM-RPG systems. First, through rigorous mathematical derivation, it establishes that the transient characteristics of paralleled systems can still be effectively characterized by a second-order motion equation. Subsequently, by applying the extended equal area criterion (EEAC) and numerical solutions to differential equations, the study uncovers the governing principles behind the variations in the critical clearing angle (CCA) and critical clearing time (CCT) for the paralleled GFM-RPG system under various operating conditions. Finally, to mitigate potential instability risks, two corrective strategies, namely adaptive damping enhancement and power switching control, are proposed to improve the transient stability of the paralleled system during symmetrical faults. Simulation results confirm the accuracy of the theoretical analysis and demonstrates the effectiveness of the proposed strategy.**

***Index Terms*—Grid-forming, renewable power generation, transient, stability control strategy.**

NOMENCLATURE

A. Variables

$\vec{E}, E, \delta$	vectors, amplitude, and phase angle of inherent voltage
$Z, Z_{\mathrm{L}}, Z_{\mathrm{F}}$	line impedance, load impedance, and fault impedance
$\omega, \omega_{\mathrm{g}}, \omega_{\mathrm{b}}$	GFM-RPG's output angular frequency, rated angular frequency, and angular frequency base value
$P_{\mathrm{ref}}, Q_{\mathrm{ref}}$	active and reactive power reference value
$P_{\mathrm{e}}, Q_{\mathrm{e}}$	active and reactive power output value
J, D	virtual inertia and damping coefficient
K_{q}	proportional coefficient of reactive power control loop
E_0, E_{ref}	rated and reference voltage amplitude
C_{f}, L_{f}	filter capacitor and inductance

B. Subscripts

n, f	normal and fault conditions

I. INTRODUCTION

In recent years, the rapid advancement of renewable energy technologies has led to a substantial increase in the integration of renewable energy sources into power systems [1]–[3]. Owing to their fast switching speeds and flexible control capabilities, power electronic devices offer distinct advantages in enhancing power quality and advancing smart grid construction [4]. However, their inherently low inertia and insufficient damping characteristics present significant stability challenges when subjected to disturbances, posing serious risks to the safety and reliability of the power supply [5]–[7]. To improve the weak disturbance immunity of power electronic devices, grid-forming (GFM) control, incorporating inertia and damping mechanisms, has been developed [8]. By simulating the external characteristics of traditional synchronous generators (SG), renewable power generation (RPG) can actively regulate both frequency and voltage. Consequently, grid-forming renewable power generation (GFM-RPG) is capable of functioning in isolated islands [9]–[10]. However, given that GFM-RPG retains the control characteristics of a power electronic device, its anti-interference ability is far inferior to that of SG. Under extreme conditions, such as short-circuit faults, GFM-RPG remains vulnerable to instability, presenting considerable risks [11].

Received: November 15, 2024
Accepted: March 23, 2025
Published Online: September 1, 2025
Sen Huang is with State Key Laboratory of Power Transmission Equipment Technology, School of Electrical Engineering, Chongqing University, Chongqing 400044, China; and also with School of Electrical Engineering, Chongqing Electric Power College, Chongqing 400053, China (e-mail: huangsenwarm@163.com).

Jun Yao (corresponding author), Wenwen He, Dong Yang, and Hai Xie are with State Key Laboratory of Power Transmission Equipment Technology, School of Electrical Engineering, Chongqing University, Chongqing 400044, China (e-mail: jyao@cqu.edu.cn; 202111021023@stu.cqu.edu.cn; yd13681553151@163.com; xihao0147@163.com).
DOI: 10.23919/PCMP.2024.000289

Currently, stability concerns associated with GFM-RPG have garnered extensive attention from both academia and industry. Utilizing impedance analysis and state-space method [12]–[15], various studies have determined that factors such as grid strength, power loop control parameters, system operating points, and the voltage control loop all play pivotal roles in influencing the stability of grid-connected GFM-RPG. References [16] and [17] highlight that the synchronization stability of GFM-RPG under minor disturbances can be improved through the optimization of controller parameters and the integration of supplementary controllers.

In addition, some scholars have investigated the transient stability issue of GFM-RPG under significant disturbances. Reference [9] analyzes the impact of reactive power voltage droop on the stability of GFM-RPG, revealing that this interaction leads to a reduction in the transient stability margin of the converter. Reference [18] asserts that non-inertial GFM-RPG can reliably transition to a new operating status as long as an equilibrium point exists. Utilizing the phase portrait method, reference [19] investigates the transient stability of four different GFM-RPG types, elucidates the impact of controller gain and virtual inertia, and subsequently proposes guidelines for controller parameter design criteria for GFM-RPG. Reference [20] employs the Lyapunov direct method to derive sufficient conditions for ensuring the transient stability of GFM-RPG control parameters. However, accurately formulating the Lyapunov function for nonlinear systems remains a complex challenge. To address the conservatism issue associated with the traditional equal area criterion (EAC), references [21] and [22] introduce the concept of a damping area and develop a more accurate method for assessing transient stability by intuitively evaluating the damping effect. Furthermore, references [23] and [24] conduct a comprehensive investigation into the transient operational characteristics of GFM-RPG following its transition from voltage-source mode to current source mode. Their findings indicate that current saturation negatively impacts system stability by constraining the stability region and deteriorating transient stability. However, the above-mentioned studies focus on a single-machine infinite-bus system, making their conclusions inapplicable for direct extrapolation to a multi-machine system.

To further enhance the transient stability of the GFM-RPG system, some control schemes have been proposed. References [9] and [25] present a control method for adaptively reducing the active power reference value of GFM-RPG to improve stability. Reference [26] proposes a mode-adaptive power angle control method, which can help GFM-RPG mitigate transient instability by toggling between positive and negative feedback modes. Meanwhile, references [27] and [28] suggest stabilization control strategies based on damping optimization, effectively contributing to overall stability enhancement. Reference [11] presents a flexible switching control method for managing inertia and damping, effectively enhancing both the critical clearing angle (CCA) and critical clearing time (CCT) simultaneously. However, beyond these control methods designed for a single-generation system mentioned above, further research is required to develop robust stabilization control strategies applicable to multi-RPG systems.

Consequently, in contrast to existing studies, this study seeks to conduct a comprehensive investigation into the transient stability analysis and corresponding control strategies for paralleled GFM-RPG systems. The main contributions of this study are presented as follows.

1) By integrating the extended equal area criterion (EEAC) with numerical solutions of differential equations, this study examines the influence of different factors on both CCA and CCT. Based on this analysis, a transient stability criterion tailored for paralleled GFM-RPG systems is established.

2) An advanced adaptive damping enhancement control method is proposed, incorporating a compensation term associated with the system power deviations within the damping control loop of GFM-RPG. This approach automatically enhances the system's damping performance while bolstering transient stability margins. In addition, an alternative power deviation switching control strategy is proposed for parallel GFM-RPG systems. By regulating unbalanced power to zero, this method effectively mitigates the risk of transient instability.

The remainder of this paper is organized as follows. Section II introduces the mathematical model of a paralleled GFM-RPG system, while Section III delves into the analysis of the transient stability mechanism and criterion. Section IV presents an adaptive damping enhancement control strategy and a power deviation switching control strategy for the paralleled system. Section V provides simulations to validate the theoretical analysis and proposed method. Finally, Section VI concludes the study.

II. MODELING OF THE PARALLELED GFM-RPG SYSTEM

A. System Description

Island microgrids play a vital role in integrating distributed renewable energy sources, offering flexible and efficient energy conversion capabilities. As a result, their development has progressed rapidly. To ensure the reliable operation of island microgrids, it is essential to examine their transient stability challenges. Consequently, this study focuses on a representative paralleled GFM-RPG system [10] as the subject of research analysis, aiming to explore its transient stability mechanism and control strategy. As illustrated in Fig. 1, the system contains two GFM-RPGs and a constant impedance load. Notably, the GFM-RPG depicted in Fig. 1 is not confined to representing a single power generation unit; instead, it can equivalently model an entire renewable energy power generation station or a coordinated cluster composed of multiple small-capacity units.

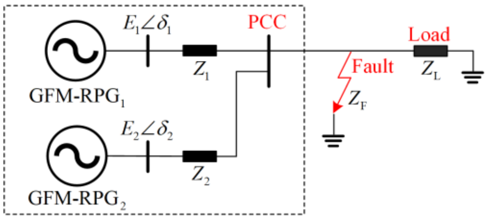

Fig. 1. Structural configuration of the paralleled GFM-RPG system.

Figure 2 shows the control block diagram of a conventional GFM-RPG [26], which consists of an external power control loop and an inner voltage and current control loop. In addition, virtual impedance is incorporated to enforce current-limiting protection for the GFM-RPG during fault conditions [9]. Since the response speed of the inner voltage and current loop is significantly higher than that of the external power loop, the dynamic behavior of the internal voltage and current control loop can be considered negligible when analyzing transient stability issues associated with the power loop [27], [28], i.e., $E = E_{\text{ref}}$ can be approximated. Consequently, the following assumptions are established:

1) The internal voltage and current controls are highly efficient and precise, enabling rapid tracking of the reference values;

2) The DC-link voltage of the GFM-RPG remains constant, as the integrated chopper circuit effectively regulates the DC-link voltage level even during faults.

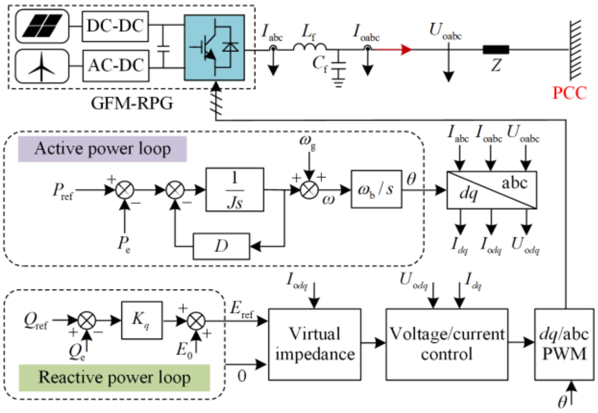

Fig. 2. Control block framework for a typical GFM-RPG system.

B. Network Voltage Equation

Because GFM-RPG exhibits a voltage source characteristic, the equivalent circuit representation of the paralleled GFM-RPG system can be derived, as illustrated in Fig. 3.

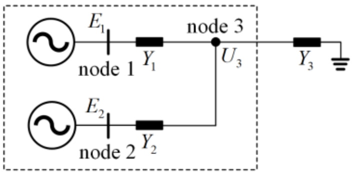

Fig. 3. Equivalent circuit model based on the paralleled GFM-RPG system.

Based on Fig. 1, the admittance in the equivalent circuit is expressed as:

$$\begin{cases} Y_1 = 1/Z_1 \\ Y_2 = 1/Z_2 \\ Y_3 = 1/Z_{\text{L}} \text{ or } 1/(Z_{\text{L}}//Z_{\text{F}}) \end{cases} \tag{1}$$

Subsequently, by applying the node analysis method, the network voltage equation of the system can be derived as:

$$\begin{bmatrix} Y_1 & -Y_1 & 0 \\ -Y_1 & Y_1+Y_2+Y_3 & -Y_2 \\ 0 & -Y_2 & Y_2 \end{bmatrix} \begin{bmatrix} E_1 \\ U_3 \\ E_2 \end{bmatrix} = \begin{bmatrix} I_1 \\ I_3 \\ I_2 \end{bmatrix} \tag{2}$$

where Y_1, Y_2, Y_3 represent the corresponding admittance, respectively; I_1, I_2, and I_3 signify the injection current of node 1, node 2, and node 3, respectively.

C. Mathematical Model of GFM-RPG

The power loop serves as a crucial control link in GFM-RPG. In conjunction with Fig. 2, the basic mathematical model of GFM-RPG can be formulated as:

$$J\mathrm{d}\omega/\mathrm{d}t = P_{\text{ref}} - P_{\text{e}} - D(\omega - \omega_{\text{g}}) \tag{3}$$

$$E = K_{\text{q}}(Q_{\text{ref}} - Q_{\text{e}}) + E_0 \tag{4}$$

Then, based on Fig. 3 and (1), the output active power of GFM-RPG$_1$ and GFM-RPG$_2$ can be derived as:

$$P_{\text{e}1} = E_1^2 G_{11} + E_1 E_2 |Y_{12}| \cos(\delta_1 - \delta_2 - \theta_{12}) \tag{5}$$

$$P_{\text{e}2} = E_2^2 G_{22} + E_2 E_1 |Y_{21}| \cos(\delta_2 - \delta_1 - \theta_{12}) \tag{6}$$

where G_{11} and G_{22} refer to the real parts of Y_{11} and Y_{22}, respectively; $|Y_{12}|$ and θ_{12} imply the amplitude and phase of Y_{12}, respectively; while $|Y_{21}|$ and θ_{21} denote the amplitude and phase of Y_{21}, respectively.

$$\begin{aligned} Y_{11} &= G_{11} + \mathrm{j}B_{11} = \frac{(Y_2+Y_3)Y_1}{Y_1+Y_2+Y_3} = |Y_{11}|\angle\theta_{11} \\ Y_{12} &= G_{12} + \mathrm{j}B_{12} = -\frac{Y_1 Y_2}{Y_1+Y_2+Y_3} = |Y_{12}|\angle\theta_{12} = Y_{21} \\ Y_{22} &= G_{22} + \mathrm{j}B_{22} = \frac{(Y_1+Y_3)Y_2}{Y_1+Y_2+Y_3} = |Y_{22}|\angle\theta_{22} \end{aligned} \tag{7}$$

D. Model of the Paralleled GFM-RPG System

The voltage vector relationship between GFM-RPG$_1$ and GFM-RPG$_2$ is illustrated in Fig. 4, where axis (d_1q_1) and axis (d_2q_2) refer to their respective reference frames, which rotate at angular frequency ω_1 and ω_2, respectively.

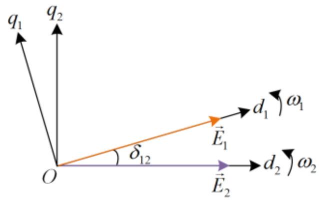

Fig. 4. Voltage vector relationship.

To analyze the synchronization characteristics of the two GFM-RPGs within the paralleled system, the following definitions are established:

$$\delta_{12} = \delta_1 - \delta_2 \tag{8}$$

$$\omega_{12} = \omega_1 - \omega_2 \tag{9}$$

where

$$\dot{\delta}_{12} = \mathrm{d}\delta_{12} / \mathrm{d}t = \omega_b \omega_{12} \tag{10}$$

Subsequently, by combining (3)–(10), the equivalent motion equation governing the overall parallel system can be formulated as:

$$J_{eq}\ddot{\delta}_{12} = P_{ref\_eq} - P_{eq} - D_{eq}\dot{\delta}_{12} \tag{11}$$

where J_{eq}, D_{eq}, P_{ref_eq}, and P_{eq} signify the equivalent inertia, damping, active power reference value, and active power output value of the paralleled system, respectively. To ensure a conservative and realistic analysis, the smaller value between $J_{eq}D_1/J_1$ and $J_{eq}D_2/J_2$ is chosen as D_{eq}.

$$\begin{cases} J_{eq} = \dfrac{J_1 J_2}{(J_1 + J_2)\omega_b} \\ D_{eq} = \min\left\{ J_{eq}\dfrac{D_1}{J_1}, J_{eq}\dfrac{D_2}{J_2} \right\} \end{cases} \tag{12}$$

$$P_{ref\_eq} = \frac{J_2}{J_1 + J_2}P_{ref1} - \frac{J_1}{J_1 + J_2}P_{ref2} \tag{13}$$

$$\begin{aligned} P_{eq} = {} & \frac{J_2}{J_1 + J_2}\left[E_1^2 G_{11} + E_1 E_2 |Y_{12}| \cos(\delta_{12} - \theta_{12})\right] - \\ & \frac{J_1}{J_1 + J_2}\left[E_2^2 G_{22} + E_2 E_1 |Y_{21}| \cos(\delta_{12} + \theta_{12})\right] \end{aligned} \tag{14}$$

Based on (8)–(14), it can be seen that the synchronization characteristics of a paralleled GFM-RPG system can still be characterized using second-order motion equations. Consequently, it is reasonable to infer that the transient stability mechanism of the paralleled system resembles those of traditional power systems. This similarity suggests that the established analytical methods for evaluating transient synchronization in traditional power systems remain applicable.

III. TRANSIENT STABILITY ANALYSIS

In the traditional transient stability analysis theory of power systems, multiple machines are typically represented as an equivalent to the single-machine infinite-bus system. The system's transient stability is assessed by comparing the acceleration area during a fault with the deceleration area after fault clearance. This approach, known as EEAC, serves as a method for determining system stability. Since GFM-RPG emulates the external dynamic characteristics of SG, this method can similarly be applied to the paralleled GFM-RPG systems investigated in this study.

A. Extended Equal Area Method

1) Without Considering Damping Term

Since this method neglects the influence of damping, the equivalent motion equation governing the paralleled GFM-RPG system can be expressed as:

$$J_{eq}\ddot{\delta}_{12} = P_{ref\_eq} - P_{eq} \tag{15}$$

According to (15) and the parameter values provided in Table AI in Appendix A, the synchronization process of the paralleled system under varying fault-clearing times can be obtained. As illustrated in Fig. 5, point A refers to the initial operating point and point C signifies the fault clearing point.

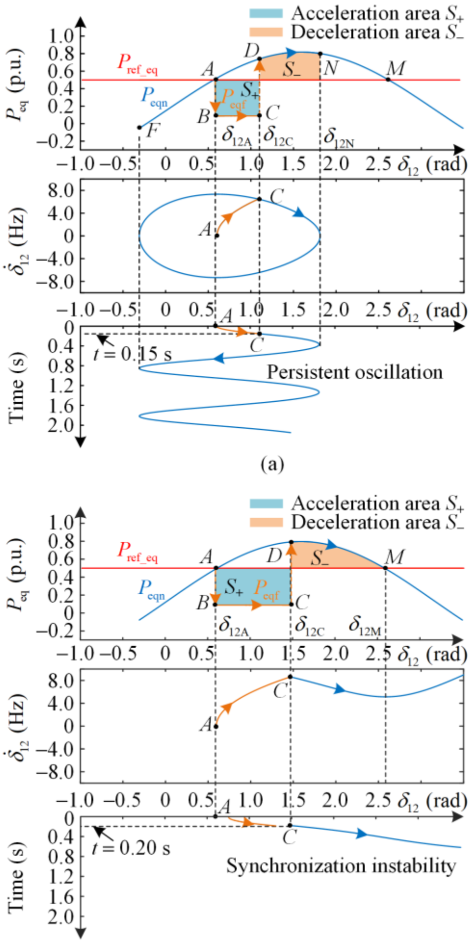

(a)

(b)

Fig. 5. Synchronization behavior of the paralleled system under different fault clearing times without considering the damping effect. (a) Fault clearing time $t = 0.15$ s. (b) Fault clearing time $t = 0.20$ s.

Figure 5(a) shows that the paralleled system maintains transient stability when the fault clearance time is 0.15 s. Following the occurrence of a symmetrical fault, the system's operating point jumps from A to B. Since $P_{ref\_eq} > P_{eq}$, the system undergoes an acceleration process. Subsequently, upon fault clearance, the operating point jumps from C to D. At this stage, as $P_{ref\_eq} < P_{eq}$, the system enters a deceleration operation stage, where the incremental kinetic energy is converted into potential energy. Since the system lacks a damping term, it undergoes a continuous exchange between kinetic energy and potential energy. Resultantly, the system reciprocates along $N \to D \to A \to F \to A \to D \to N$, maintaining a state of critical equilibrium.

Figure 5(b) shows that the paralleled system experiences instability when the fault clearance time reaches 0.2 s. The long duration of the fault prevents the system from generating sufficient deceleration area to offset the increase in kinetic energy. Consequently, once the operating point crosses point *M*, the system loses stability due to uncontrollable sliding motion.

The above discussions provide a qualitative analysis of transient instability, while the quantitative evaluation of the stability of the paralleled system can conducted utilizing EEAC, i.e.:

$$\max\{S_-\} \geqslant S_+ \tag{16}$$

where

$$\begin{aligned} \max\{S_-\} &= \int_{\delta_{12\mathrm{C}}}^{\delta_{12\mathrm{M}}} P_{\mathrm{eqn}} - P_{\mathrm{ref\_eq}} \\ S_+ &= \int_{\delta_{12\mathrm{A}}}^{\delta_{12\mathrm{C}}} P_{\mathrm{ref\_eq}} - P_{\mathrm{eqf}} = \frac{1}{2} J_{\mathrm{eq}} \omega_{12\mathrm{C}}^2 \end{aligned} \tag{17}$$

where $\delta_{12\mathrm{A}}$, $\delta_{12\mathrm{C}}$, and $\delta_{12\mathrm{M}}$ indicate the angles of the initial equilibrium point, the fault clearing point, and the unstable equilibrium point, respectively.

2) Considering Damping Term

The above analysis neglects the influence of the damping term. However, when damping effects become significant, the resulting assessment may lead to a relatively conservative conclusion. To improve the accuracy of the analysis, this section employs the EEAC method while incorporating damping to analyze the transient synchronization stability mechanism of the paralleled system.

First, equation (11) can be rewritten as:

$$J_{\mathrm{eq}} \dot{\delta}_{12} = P_{\mathrm{m\_eq}} - P_{\mathrm{eq}} \tag{18}$$

where

$$P_{\mathrm{m\_eq}} = P_{\mathrm{ref\_eq}} - D_{\mathrm{eq}} \dot{\delta}_{12} \tag{19}$$

According to (18), the synchronization process of the paralleled system, considering the damping effects under varying fault clearing times, can be derived, as illustrated in Fig. 6.

In contrast to Fig. 5(b), Fig. 6(a) shows that the paralleled system maintains transient stability even when the fault-clearing time is 0.20 s. Following the occurrence of a symmetrical fault, the system's operating point jumps from *A* to *B*. Although condition $P_{\mathrm{m\_eq}} > P_{\mathrm{eq}}$ remains valid, the acceleration area S_+ decreases as a result of the dynamic decline in $P_{\mathrm{m\_eq}}$. Subsequently, once the fault is cleared, the system's operating point jumps from *C* to *D*. Given that $P_{\mathrm{m\_eq}} < P_{\mathrm{eq}}$, the system shifts into a deceleration operation stage. Consequently, due to the influence of the damping component, it ultimately stabilizes at its initial equilibrium point *A*.

Figure 6(b) shows the occurrence of transient instability phenomenon when the fault clearing time is set to 0.3 s. As the fault persists for a longer duration, even with a moderate reduction in $P_{\mathrm{m\_eq}}$, the paralleled system still lacks sufficient deceleration area S_- to offset the increase in kinetic energy. Once the operating point surpasses point *M*, δ_{12} continues to increase, leading to a loss of synchronization within the paralleled system.

A comparative analysis of the above-mentioned two parts reveals that the damping term plays a crucial role in significantly enhancing the CCT of the paralleled system while improving its transient stability. Therefore, to prevent excessively conservative analytical results, the impact of damping on the transient stability should be fully considered.

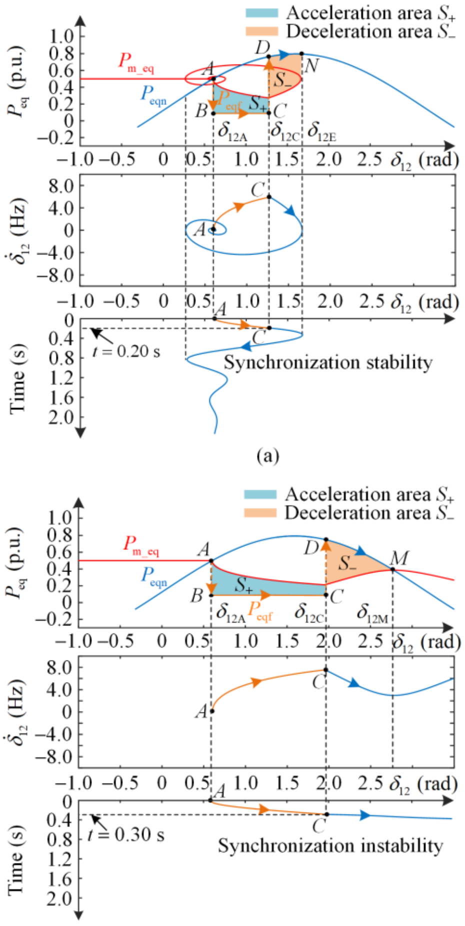

Fig. 6. Synchronization process of the paralleled system under different fault clearing times considering the damping effect. (a) Fault clearing time $t = 0.20$ s. (b) Fault clearing time $t = 0.30$ s.

Consequently, the transient stability of the paralleled system must satisfy the conditions:

$$\underbrace{\int_{\delta_{12\mathrm{C}}}^{\delta_{12\mathrm{M}}} P_{\mathrm{eqn}} - P_{\mathrm{m\_eq}}}_{\max\{S_-\}} \geqslant \underbrace{\int_{\delta_{12\mathrm{A}}}^{\delta_{12\mathrm{C}}} P_{\mathrm{m\_eq}} - P_{\mathrm{eqf}}}_{S_+} \tag{20}$$

B. Transient Stability Criterion

Based on the above analysis, it can be seen that an accurate evaluation of the transient stability necessitates incorporating the effect of damping. However, since the damping term is not a function of $\delta_{12\mathrm{C}}$, it cannot be directly quantified using (20). Therefore, this study adopts principles from differential equation solving techniques and employs the Runge–Kutta method to obtain the numerical solution of $[\delta_{12}, \dot{\delta}_{12}]$, followed by numerical fitting to establish its corresponding analytical expression of $\dot{\delta}_{12}-\delta_{12}$. Building on this approach, a more accurate criterion for transient stability can be obtained.

Equation (11) can be interpreted as a second-order differential equation with constant coefficients. Since direct computation is challenging due to the presence of a second-order derivative term, converting the second-order derivative term into a first-order derivative is preferable. Therefore, the following transformation can be introduced.

$$\begin{cases} x(1)=\delta_{12} \\ x(2)=\dot{x}(1)=\dot{\delta}_{12} \end{cases} \tag{21}$$

Subsequently, equation (11) can be written as a system using first-order differential equations.

$$\begin{cases} \dot{x}(1)=x(2)=f_1\big(t,x(1),x(2)\big) \\ \dot{x}(2)=\Big\{P_{\mathrm{ref\_eq}}-\dfrac{J_2}{J_1+J_2}\big[E_1^2G_{11}+E_1E_2|Y_{12}|\cos(x(1)-\theta_{12})\big]+ \\ \quad \dfrac{J_1}{J_1+J_2}\big[E_2^2G_{22}+E_2E_1|Y_{21}|\cos(x(1)+\theta_{12})\big]-D_{\mathrm{eq}}x(2)\Big\}/ \\ \quad J_{\mathrm{eq}}=f_2\big(t,x(1),x(2)\big) \\ x_0(1)=\delta_{12\mathrm{A}} \\ x_0(2)=0 \end{cases} \tag{22}$$

where $x_0(1)$ indicates the initial value of δ_{12}; and $x_0(2)$ signifies the initial value of $\dot{\delta}_{12}$. Subsequently, the Runge–Kutta method can be used to iteratively solve (22), with the specific formula given as follows:

$$\begin{cases} x_{i+1}(1)=x_i(1)+(K_{11}+2K_{12}+2K_{13}+K_{14})/6 \\ x_{i+1}(2)=x_i(2)+(K_{21}+2K_{22}+2K_{23}+K_{24})/6 \end{cases} \tag{23}$$

The solution expression for each parameter is given by:

$$\begin{cases} K_{11}=f_1\big(t,x_i(1),x_i(2)\big) \\ K_{21}=f_2\big(t,x_i(1),x_i(2)\big) \\ K_{12}=f_1\big(t+h/2,x_i(1)+h/2\cdot K_{11},x_i(2)+K_{21}\cdot h/2\big) \\ K_{22}=f_2\big(t+h/2,x_i(1)+K_{11}\cdot h/2,x_i(2)+K_{21}\cdot h/2\big) \\ K_{13}=f_1\big(t+h/2,x_i(1)+K_{12}\cdot h/2,x_i(2)+K_{22}\cdot h/2\big) \\ K_{23}=f_2\big(t+h/2,x_i(1)+K_{12}\cdot h/2,x_i(2)+K_{22}\cdot h/2\big) \\ K_{14}=f_1\big(t+h,x_i(1)+hK_{13},x_i(2)+hK_{23}\big) \\ K_{24}=f_2\big(t+h,x_i(1)+hK_{13},x_i(2)+hK_{23}\big) \end{cases} \tag{24}$$

where h refers to the calculation step size. By integrating the above-mentioned calculation process, the numerical solution of $[\delta_{12}, \dot{\delta}_{12}]$ can be calculated. Subsequently, the analytical expression of $\dot{\delta}_{12}-\delta_{12}$ can be obtained through curve fitting. Since this study primarily focuses on the first-swing stability of the power angle, the fitting range is defined as $[\delta_{12\mathrm{A}}, \pi]$. Using the parameters listed in Table AI in Appendix A as a reference, the fitting results under different conditions can be obtained, as shown in Fig. 7.

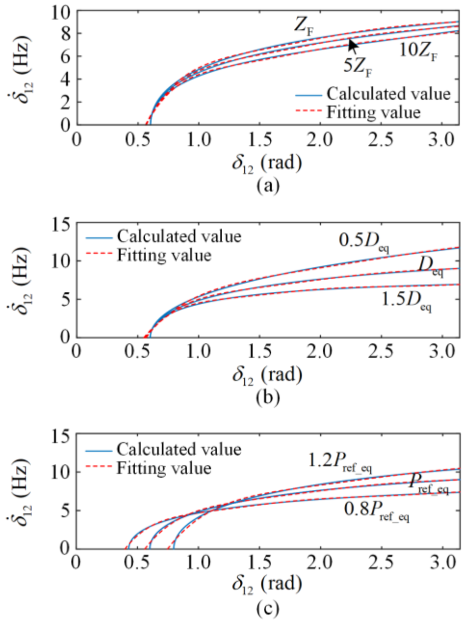

Fig. 7. Fitting results across various scenarios. (a) Different fault impedance. (b) Different equivalent damping. (c) Different equivalent active power reference value.

To enhance the accuracy, a seventh-order polynomial is selected as the fitting model:

$$\begin{aligned} \dot{\delta}_{12}=g(\delta_{12})=c_7\delta_{12}^7+c_6\delta_{12}^6+c_5\delta_{12}^5+c_4\delta_{12}^4+ \\ c_3\delta_{12}^3+c_2\delta_{12}^2+c_1\delta_{12}+c_0 \end{aligned} \tag{25}$$

where c_0-c_7 represent the constants determined through fitting.

By incorporating (25), the EEAC method for judging the transient stability of the paralleled system can be yielded:

$$\underbrace{\int_{\delta_{12\mathrm{A}}}^{\delta_{12\mathrm{C}}} P_{\mathrm{ref\_eq}}-P_{\mathrm{eqf}}-D_{\mathrm{eq}}g(\delta_{12})\mathrm{d}\delta_{12}}_{S_+}=\underbrace{\int_{\delta_{12\mathrm{C}}}^{\delta_{12\mathrm{M}}} P_{\mathrm{eqn}}-P_{\mathrm{ref\_eq}}\mathrm{d}\delta_{12}}_{\max\{S_-\}} \tag{26}$$

where $\delta_{12\mathrm{A}}$ and $\delta_{12\mathrm{M}}$ can be obtained by solving $P_{\mathrm{ref\_eq}}-P_{\mathrm{eqn}}=0$.

Based on (25) and (26), the following equation can be given:

$$\begin{aligned} -P_{\mathrm{Tf}}\delta_{12\mathrm{A}}+P_{\mathrm{Tn}}\delta_{12\mathrm{M}}+H_{12\mathrm{f}}\sin(\delta_{12\mathrm{A}}-\theta_{12\mathrm{f}})- \\ H_{21\mathrm{f}}\sin(\delta_{12\mathrm{M}}+\theta_{12\mathrm{f}})-H_{12\mathrm{n}}\sin(\delta_{12\mathrm{M}}-\theta_{12\mathrm{n}})+ \\ H_{21\mathrm{n}}\sin(\delta_{12\mathrm{M}}+\theta_{12\mathrm{n}})-H_{12\mathrm{f}}\sin(\delta_{12\mathrm{C}}-\theta_{12\mathrm{f}})+ \\ H_{21\mathrm{f}}\sin(\delta_{12\mathrm{C}}+\theta_{12\mathrm{f}})+H_{12\mathrm{n}}\sin(\delta_{12\mathrm{C}}-\theta_{12\mathrm{n}})- \\ H_{21\mathrm{n}}\sin(\delta_{12\mathrm{C}}+\theta_{12\mathrm{n}})-[F(\delta_{12\mathrm{C}})-F(\delta_{12\mathrm{A}})]=0 \end{aligned} \tag{27}$$

where the expression for each parameter is given as:

$$\begin{cases} P_{\mathrm{Tf}}=\dfrac{J_2}{J_1+J_2}P_{\mathrm{ref1}}-\dfrac{J_1}{J_1+J_2}P_{\mathrm{ref2}}-\dfrac{J_2}{J_1+J_2}E_1^2G_{11\mathrm{f}}+\dfrac{J_1}{J_1+J_2}E_2^2G_{22\mathrm{f}} \\ P_{\mathrm{Tn}}=\dfrac{J_2}{J_1+J_2}P_{\mathrm{ref1}}-\dfrac{J_1}{J_1+J_2}P_{\mathrm{ref2}}-\dfrac{J_2}{J_1+J_2}E_1^2G_{11\mathrm{n}}+\dfrac{J_1}{J_1+J_2}E_2^2G_{22\mathrm{n}} \\ H_{12\mathrm{f}}=\dfrac{J_2}{J_1+J_2}E_1E_2|Y_{12\mathrm{f}}| \\ H_{12\mathrm{n}}=\dfrac{J_2}{J_1+J_2}E_1E_2|Y_{12\mathrm{n}}| \\ H_{21\mathrm{f}}=\dfrac{J_1}{J_1+J_2}E_2E_1|Y_{12\mathrm{f}}| \\ H_{21\mathrm{n}}=\dfrac{J_1}{J_1+J_2}E_2E_1|Y_{12\mathrm{n}}| \\ F(\delta_{12\mathrm{C}})=D_{\mathrm{eq}}\left[\dfrac{c_7}{8}\delta_{12\mathrm{C}}^8+\dfrac{c_6}{7}\delta_{12\mathrm{C}}^7+\dfrac{c_5}{6}\delta_{12\mathrm{C}}^6+\dfrac{c_4}{5}\delta_{12\mathrm{C}}^5+\right. \\ \qquad \left.\dfrac{c_3}{4}\delta_{12\mathrm{C}}^4+\dfrac{c_2}{3}\delta_{12\mathrm{C}}^3+\dfrac{c_1}{2}\delta_{12\mathrm{C}}^2+c_0\delta_{12\mathrm{C}}\right] \\ F(\delta_{12\mathrm{A}})=D_{\mathrm{eq}}\left[\dfrac{c_7}{8}\delta_{12\mathrm{A}}^8+\dfrac{c_6}{7}\delta_{12\mathrm{A}}^7+\dfrac{c_5}{6}\delta_{12\mathrm{A}}^6+\dfrac{c_4}{5}\delta_{12\mathrm{A}}^5+\right. \\ \qquad \left.\dfrac{c_3}{4}\delta_{12\mathrm{A}}^4+\dfrac{c_2}{3}\delta_{12\mathrm{A}}^3+\dfrac{c_1}{2}\delta_{12\mathrm{A}}^2+c_0\delta_{12\mathrm{A}}\right] \end{cases} \tag{28}$$

From (27), $\delta_{12\mathrm{C}}$ can be treated as the unknown variable in a nonlinear function, which can be calculated using the Newton-Raphson method. Figure 8 shows the variation curve of CCA under different operating conditions. The results demonstrate that an increase in the fault impedance or system damping leads to a larger CCA, whereas an increase in the equivalent active power reference value results in a decrease in CCA.

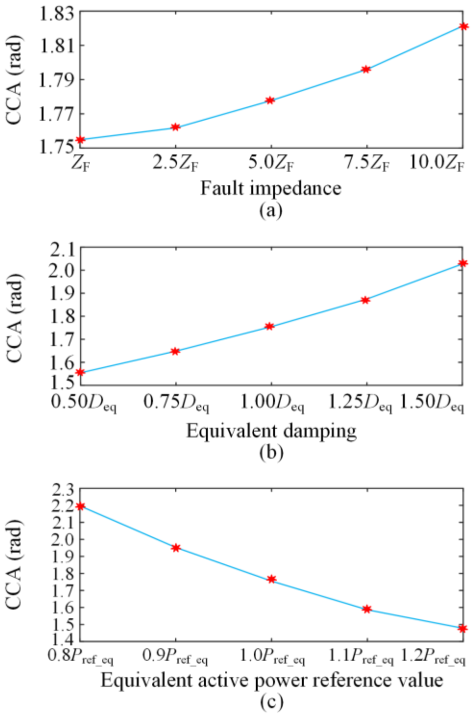

Fig. 8. Variation curve of the CCA across different scenarios. (a) Different fault impedance. (b) Different equivalent damping. (c) Different equivalent active power reference value.

In traditional transient stability analysis theory, CCT is considered more intuitive than CCA, making it a more appropriate criterion for assessing transient stability. By incorporating the calculation results of the Runge-Kutta method, the CCT corresponding to CCA under different impedances can be determined, as shown in Fig. 9. Similar to the variation pattern of CCA, an increase in fault impedance or damping results in an extended CCT. Conversely, a higher equivalent active power reference value leads to a smaller CCT.

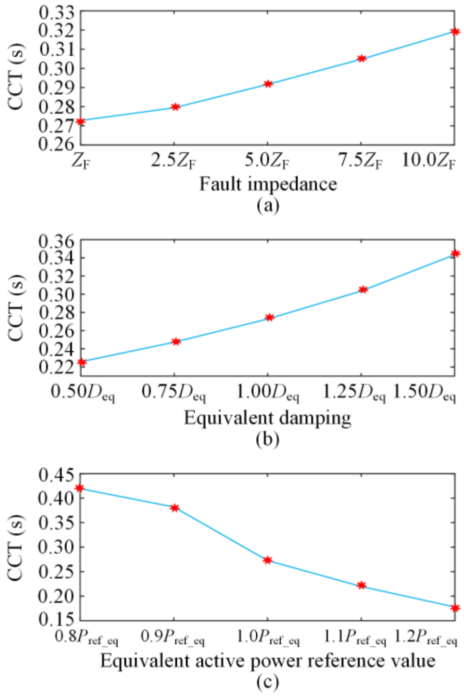

Fig. 9. Variation curve of the CCT across different scenarios. (a) Different fault impedance. (b) Different equivalent damping. (c) Different equivalent active power reference value.

Building on the above analysis, to ensure transient stability in a paralleled system experiencing symmetrical faults, the fault clearing time t_{c} must meet the following criterion:

$$t_{\mathrm{c}} \leqslant \mathrm{CCT} \tag{29}$$

From (29), a criterion for assessing the transient stability of the paralleled system can be established. If the fault clearing time t_{c} is less than CCT, the system is considered stable. On the contrary, if the fault clearing time t_{c} surpasses CCT, the system is at high risk of transient synchronization instability.

IV. TRANSIENT STABILITY CONTROL STRATEGY

The transient stability criterion of the paralleled GFM-RPG system has been investigated in Section III. This section introduces the stability control strategy under symmetrical fault conditions, focusing on the two aspects of damping enhancement and power control.

A. Adaptive Damping Enhancement Control Strategy

From the previous analysis in Section III, it can be seen that the damping term positively influences the transient stability of the paralleled system. Moreover, unlike SG, where damping is inherently dictated by structural properties, the damping characteristics of GFM-RPG can be dynamically adjusted through control parameters. Therefore, this section introduces an adaptive damping enhancement control strategy, using real-time adjustments to the damping coefficient to improve system stability. The control block diagram is shown in Fig. 10, and its implementation steps are outlined as follows.

Step 1: Gather the reference and output values of active power for each GFM-RPG and feed them into the active power control loop.

Step 2: Calculate $\left|P_{\mathrm{ref\_eq}}-P_{\mathrm{eqf}}\right|/P_{\mathrm{eqf}}$ based on (13) and (14), then transmit the computed results to the damping control link.

Step 3: Derive the output $D\left|P_{\mathrm{ref\_eq}}-P_{\mathrm{eqf}}\right|/P_{\mathrm{eqf}}$ from the additional damping control link, and subsequently use it to adjust the damping characteristics of the GFM-RPG system.

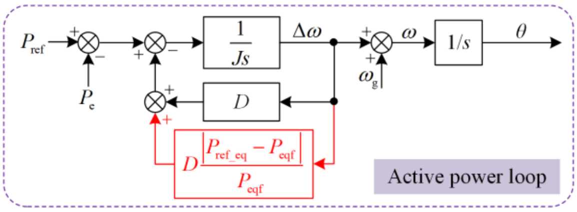

Fig. 10. Block diagram based on the control framework for the adaptive damping enhancement.

According to (1), (7), and (14), when the fault occurs, P_{eqf} decreases, leading to an increase in the ratio of $\left|P_{\mathrm{ref\_eq}}-P_{\mathrm{eqf}}\right|/P_{\mathrm{eqf}}$. This observation enhances the damping of the paralleled system, thereby strengthening its ability to suppress disturbances. Following a similar derivation process expressed in (8)–(14), the equivalent motion equation of the paralleled system incorporating the enhanced damping control strategy can be yielded:

$$J_{\mathrm{eq}}\ddot{\delta}_{12}=P_{\mathrm{ref\_eq}}-P_{\mathrm{eq}}-D_{\mathrm{eq}}\left(1+\frac{\left|P_{\mathrm{ref\_eq}}-P_{\mathrm{eqf}}\right|}{P_{\mathrm{eqf}}}\right)\dot{\delta}_{12} \quad (30)$$

In addition, utilizing the Runge-Kutta method, the analytical expression of $\dot{\delta}_{12}-\delta_{12}$ with the damping enhancement control strategy can be obtained through fitting. Figure 11 shows the fitting results under different operating conditions.

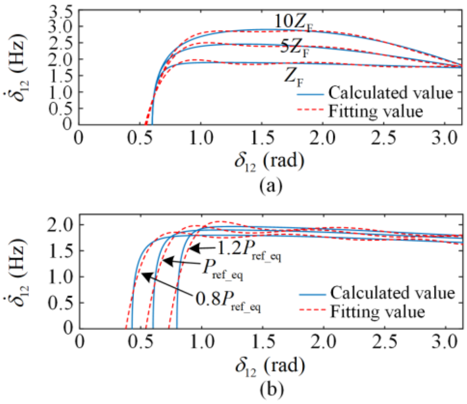

(a)

(b)

Fig. 11. Fitting results under varying conditions with the applied damping enhancement control strategy. (a) Different fault impedance. (b) Different equivalent active power reference value.

Figure 12 shows the variation curves of CCA and CCT under different conditions, with and without the implementation of the damping enhancement control strategy. It can be seen that the adoption of the proposed strategy leads to a substantial increase in both CCA and CCT, thereby significantly improving the transient stability margin of the system.

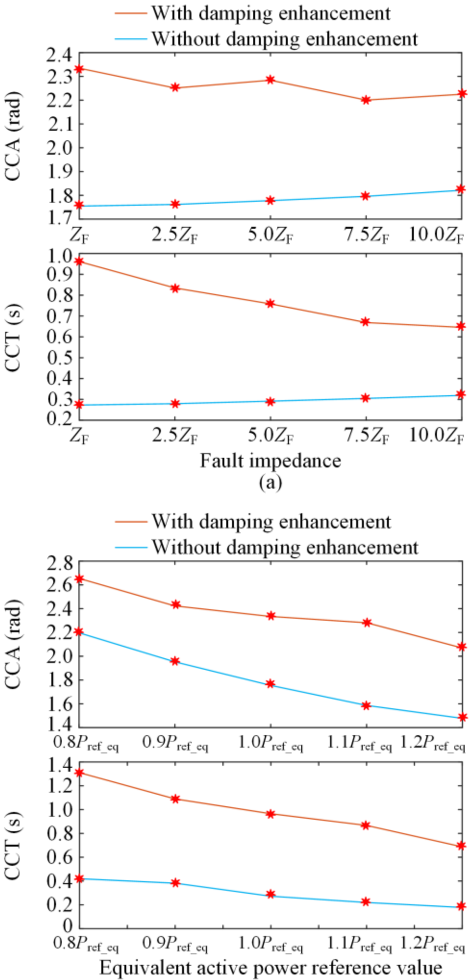

(a)

(b)

Fig. 12. Variation curve of the CCA and CCT with or without the damping enhancement control strategy across different scenarios. (a) Different fault impedance. (b) Different equivalent active power reference value.

If a system comprises numerous converters with significant differences in control parameters and operating modes, it becomes challenging to determine $P_{\mathrm{ref\_eq}}$ and P_{eqf}. Consequently, the stability control method may fail to function effectively. To solve this problem, the output of the additional damping control circuit is changed to $D\left|P_{\mathrm{ref}}-P_{\mathrm{e}}\right|/P_{\mathrm{e}}$, maintaining the same working principle as the one mentioned above. Following the occurrence of a short-circuit fault, the actual output power P_{e} of GFM-RPG decreases, deviating from the reference power value P_{ref} ($P_{\mathrm{ref}}\neq P$). As a result, the condition $\left|P_{\mathrm{ref}}-P_{\mathrm{e}}\right|/P_{\mathrm{e}}>0$ is met, thereby activating the damping control circuit.

Without the need for centralized control at the system level, additional damping can be introduced based on variations in the converters' own active power output. This approach effectively enhances the damping characteristics of GFM-RPG while simultaneously strengthening the transient stability of the system.

B. Power Deviation Switching Control Strategy

The core issue of transient instability arises from a mismatch between the active power reference and actual active output within a paralleled system under symmetrical faults. In other words, such power imbalance is the fundamental cause of transient instability. Therefore, the simplest method to mitigate instability is to ensure that the power deviation is reduced to zero during fault conditions, as shown in Fig. 13. This measure effectively prevents the adverse effect of power imbalance on the transient stability of the paralleled GFM-RPG system.

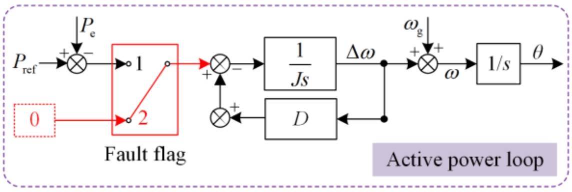

Fig. 13. Control block diagram based on the power deviation switching control strategy.

Figure 14 shows the theoretical justification for utilizing power deviation switching control to enhance the transient stability of the paralleled system. It is observed that by setting the power deviation to zero during the fault period, the active power reference value P_{ref} effectively matches the actual active power output P_e. Consequently, this observation eliminates the acceleration area of the GFM-RPG during the fault, ensuring that both ω and δ remain unchanged from their normal status. Moreover, after the fault is cleared, the deceleration area of the GFM-RPG reaches its maximum, thereby maximizing transient stability throughout the whole fault process.

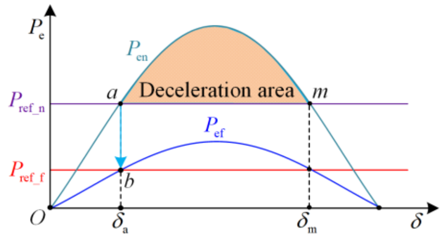

Fig. 14. P_e-δ curve embedded with power deviation switching strategy.

V. SIMULATION VERIFICATION

To validate the analytical results and the effectiveness of the proposed strategy, simulations are conducted on a paralleled GFM-RPG system using MATLAB/Simulink. The configuration of the simulated system is shown in Fig. 1, while the detailed parameters utilized in the simulation system are shown in Appendix A.

A. Simulation Validation of Transient Stability Criterion

Case 1: Figure 15(a) shows the simulation results when the fault is cleared at 0.3 s. The CCT under this condition is approximately 0.27 s, which is less than 0.3 s. Consequently, an irreversible transient instability develops after the fault. However, when the fault clearing time is reduced to 0.25 s, being lower than the CCT, the system successfully regains stability post-fault, as shown in Fig. 15(b).

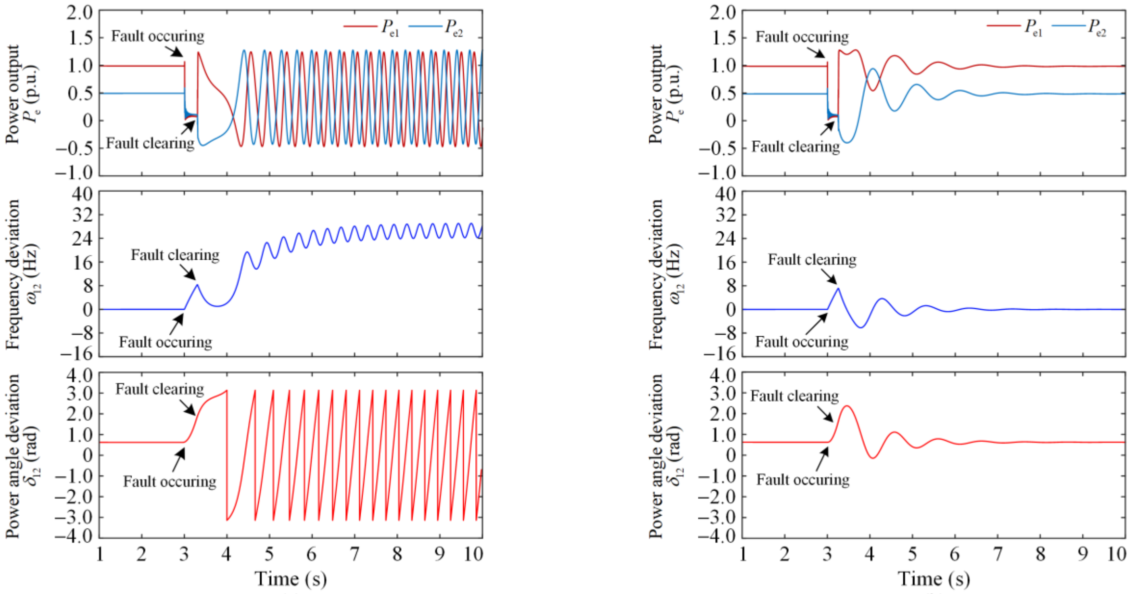

(a) (b)

Fig. 15. Simulation outcomes for Case 1. (a) Fault clearing time showing 0.3 s>CCT. (b) Fault clearing time indicating 0.25 s<CCT.

Case 2: The fault impedance is increased from Z_F to $10Z_F$. Figure 16(a) shows the simulation results when the fault clearing time is 0.35 s. Given that the CCT under this condition is about 0.32 s, lower than 0.35 s, the paralleled system experiences instability after the fault. Conversely, when the fault duration time is reduced to 0.3 s, which is less than the CCT, the system successfully retains stability after the fault, as shown in Fig. 16(b).

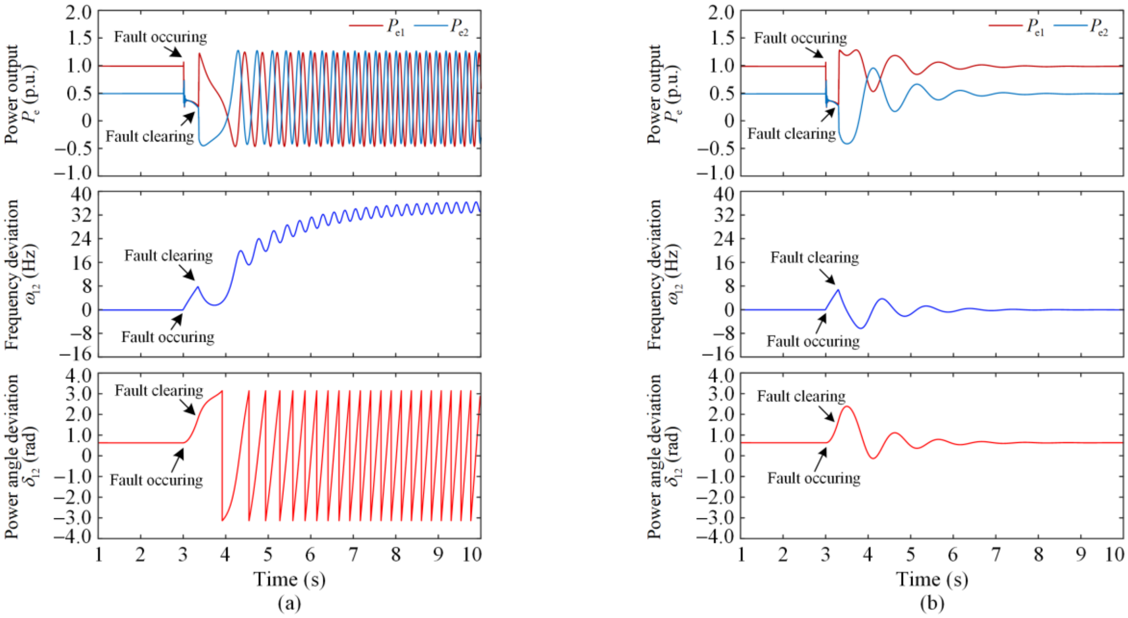

(a) (b)

Fig. 16. Simulation outcomes for Case 2. (a) Fault clearing time showing 0.35 s>CCT. (b) Fault clearing time showing 0.3 s<CCT.

Case 3: The equivalent damping parameter, initially denoted as D_{eq}, is adjusted to $1.5D_{eq}$. Figure 17(a) shows the simulation outcomes corresponding to the fault clearing time of 0.37 s. Given that the CCT in this case is approximately 0.34 s, lower than 0.37 s, the system loses stability after the fault. However, when the fault duration time is reduced to 0.33 s, which is lower than the CCT, the system successfully achieves transient stability post-fault, as shown in Fig. 17(b).

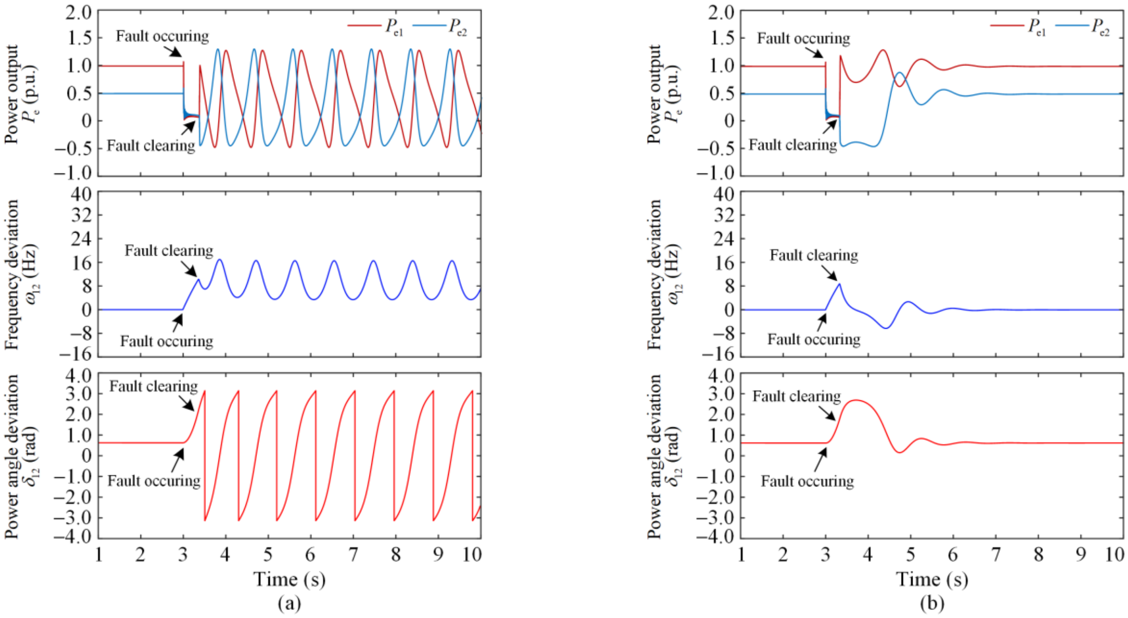

(a) (b)

Fig. 17. Simulation outcomes for Case 3. (a) Fault clearing time indicating 0.37 s>CCT. (b) Fault clearing time indicating 0.33 s<CCT.

Case 4: The equivalent active power reference value, initially represented as P_{ref_eq}, is adjusted to $1.2P_{ref\_eq}$. Figure 18(a) shows the simulation results when the fault clearing time is 0.2 s. Given that the

CCT in this case is approximately 0.178 s and is lower than 0.2 s, transient instability occurs in the system. However, when the fault duration time is reduced to 0.15 s, which falls below the CCT, the system successfully restores stability after the fault, as depicted in Fig. 18(b).

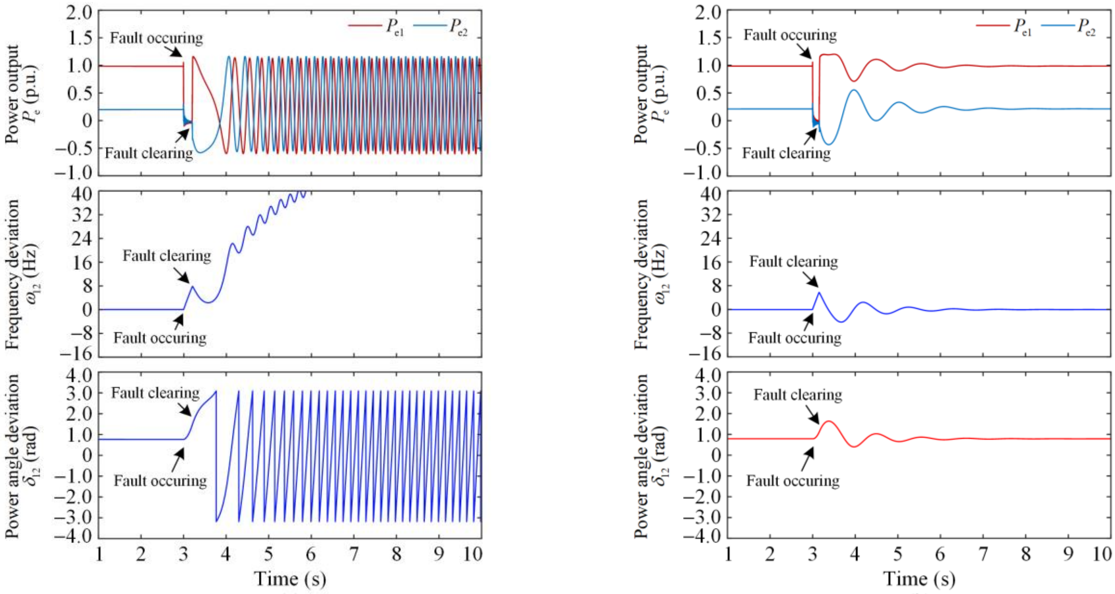

(a) (b)

Fig. 18. Simulation outcomes for Case 4. (a) Fault clearing time showing $0.2\,\text{s} > \text{CCT}$. (b) Fault clearing time indicating $0.15\,\text{s} < \text{CCT}$.

B. Simulation Validation of the Proposed Strategy in Simple Paralleled GFM-RPG System

Case 5: In this case, the fault clearing time is 0.5 s, which exceeds the CCT. As shown in Fig. 19(a), the absence of the proposed control strategy results in irreversible transient instability. Conversely, Fig. 19(b) shows the simulation results when the adaptive damping enhancement control strategy is adopted. With a substantial enhancement in damping, the system successfully restores stability after the fault. By contrast, as depicted in Fig. 19(c), the power deviation switching control strategy not only ensures transient stability but also accelerates the recovery process, resulting in a more seamless transient process.

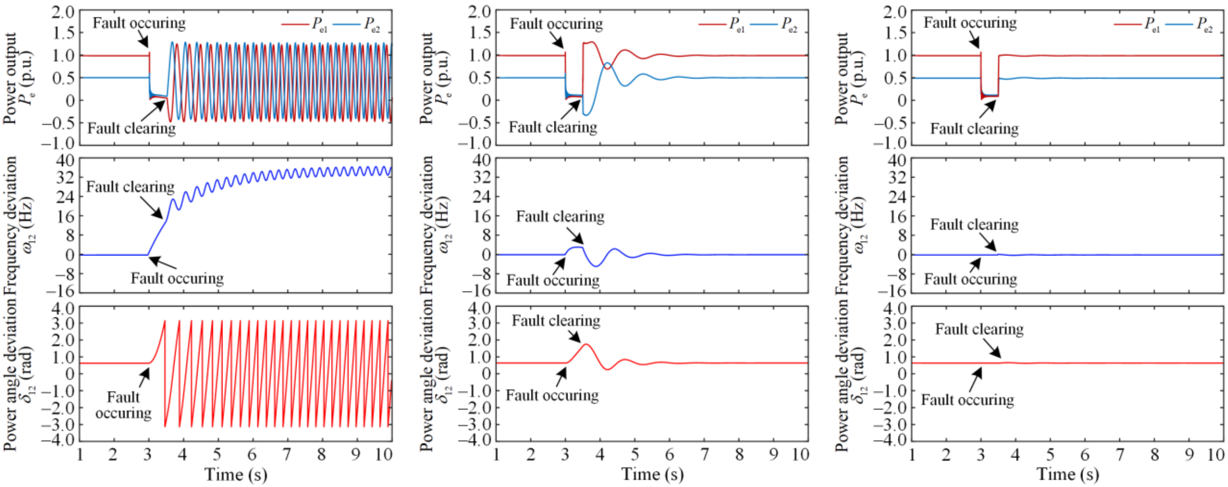

(a) (b) (c)

Fig. 19. Simulation outcomes for Case 5. (a) Without the proposed control strategy. (b) With adaptive damping enhancement control strategy. (c) With power deviation switching control strategy.

Case 6: The fault impedance is increased from Z_F to $10Z_F$, and the corresponding fault clearing time is set to 0.5 s, which exceeds the CCT. As shown in Fig. 20(a), the paralleled system exhibits instability in the absence of the proposed control strategy. Conversely, as shown in Fig. 20(b), when the adaptive damping enhancement control strategy is applied, the system regains stability within approximately one cycle of oscillation. Figure 20(c) shows the simulation results for the power deviation switching control strategy. The results indicate that this strategy maintains commendable control performance, ensuring a smooth transient response with no obvious oscillation.

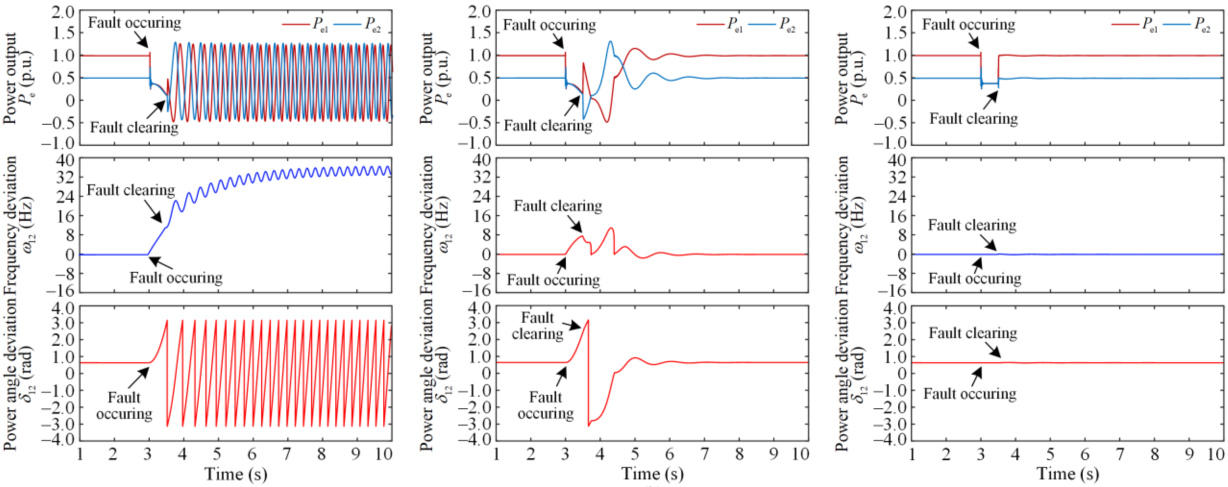

(a) (b) (c)

Fig. 20. Simulation outcomes for Case 6. (a) Without the proposed control strategy. (b) With adaptive damping enhancement control strategy. (c) With power deviation switching control strategy.

Case 7: The equivalent active power reference value is increased from $P_{\text{ref\_eq}}$ to $1.2P_{\text{ref\_eq}}$, while the fault clearing time remains 0.5 s, exceeding the CCT. As shown in Fig. 21(a), the irreversible transient instability occurs in the absence of the proposed control strategy. In contrast, the implementation of the adaptive damping enhancement control strategy shown in Fig. 21(b) facilitates the system's ability to achieve transient stability. As shown in Fig. 21(c), the integration of the power deviation switching control strategy enables the system to quickly and smoothly recover to a stable operating status.

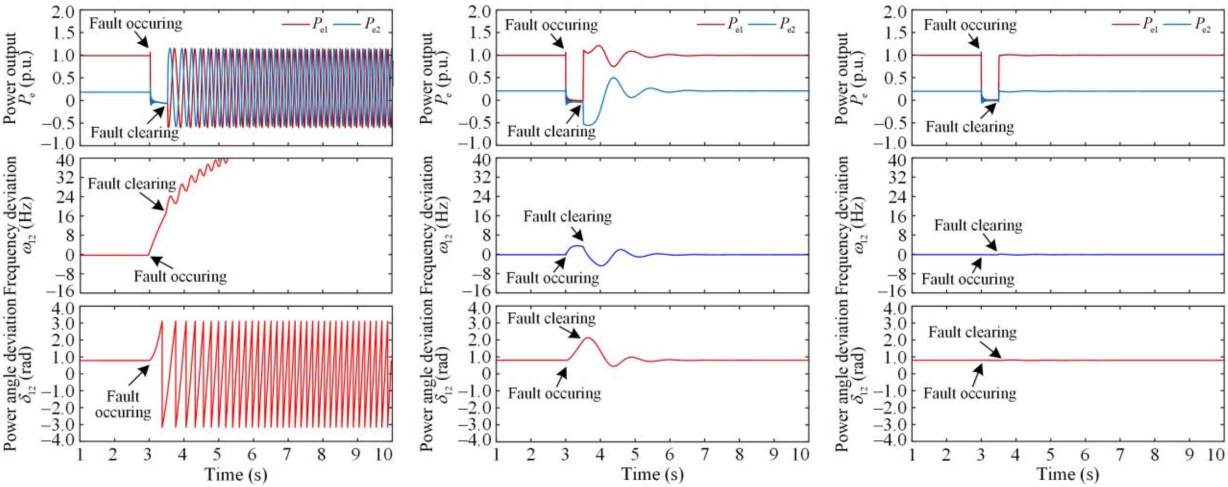

(a) (b) (c)

Fig. 21. Simulation outcomes for Case 7. (a) Without the proposed control strategy. (b) With adaptive damping enhancement control strategy. (c) With power deviation switching control strategy.

C. Simulation Validation of the Proposed Strategy in Two-area with Four-RPG System

To further validate the effectiveness of the proposed adaptive damping enhancement and power deviation switching strategies across different scenarios, this study examines a two-area system incorporating four RPGs, as shown in Fig. 22. This system consists of four GFM-RPGs, with GFM-RPG$_1$ and GFM-RPG$_2$ located in region 1, while GFM-RPG$_3$ and GFM-RPG$_4$ are situated in region 2. The specific system parameters are shown in Table A2 in Appendix A. The operating condition of the system involves a three-phase symmetrical short circuit fault occurring at the midpoint of transmission line L_8 at 1.0 s, where the fault is cleared after 0.5 s.

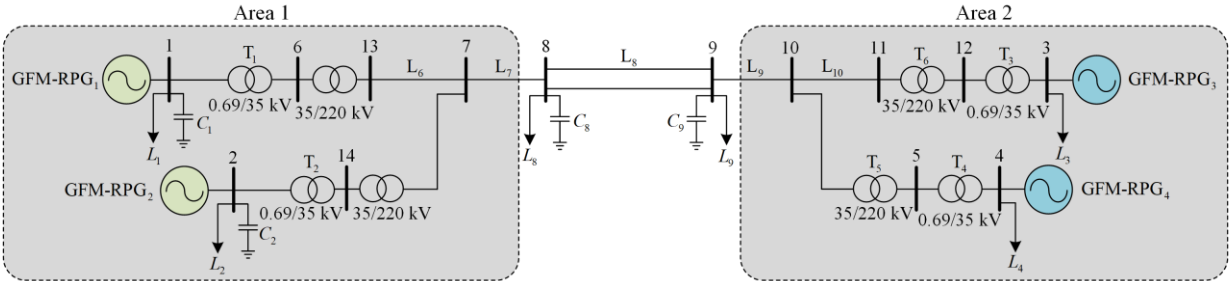

Fig. 22. Topology of the two-area system integrating four RPGs.

Case 8: Figure 23 shows the simulation results under various control strategies. Initially, when employing the traditional control strategy, the system encounters transient instability after fault clearance. This instability is depicted by the blue curve, where the output frequencies of GFM-RPG$_1$, GFM-RPG$_3$, and GFM-RPG$_4$ exhibit irreversible divergences. Due to the presence of four GFM-RPGs in the system, $\left|P_{\text{ref\_eq}}-P_{\text{eqf}}\right|/P_{\text{eqf}}$ is difficult to obtain directly. Therefore, an alternative approach is adopted which involves setting the additional damping term to $D\left|P_{\text{ref}}-P_{\text{e}}\right|/P_{\text{e}}$. By contrast, when the proposed adaptive damping enhancement control strategy is adopted, the system's transient stability exhibits significant improvement, as shown by the orange curve. Once the fault is cleared, each GFM-RPG gradually recovers its stability following a period of reduced oscillation. The red curve represents the simulated waveform obtained after adopting the power deviation switching control strategy. It can be seen that this approach facilitates a rapid and stable transient response for each GFM-RPG, with a considerable reduction in oscillation amplitude. The system maintains strong transient synchronization stability throughout the entire fault process. The above simulation analysis effectively validates the reliability of the proposed stable control strategy.

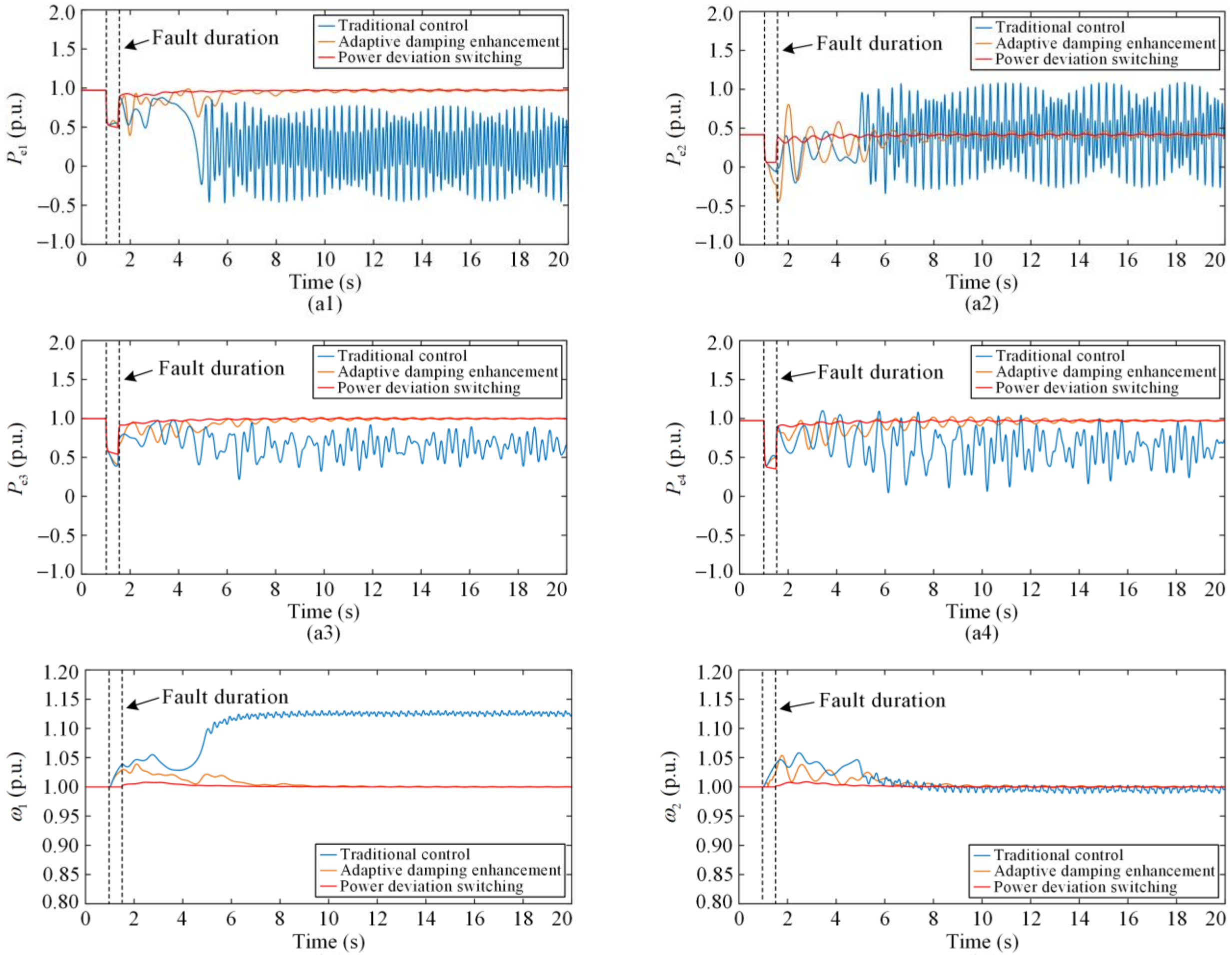

(b1) (b2)

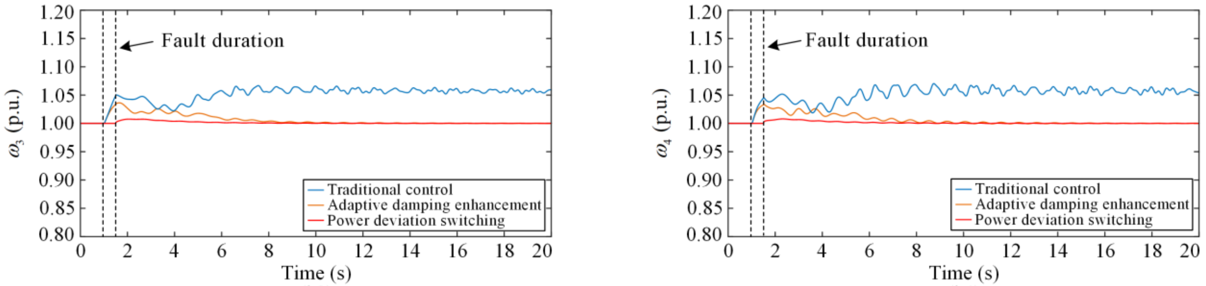

(b3) (b4)

Fig. 23. Simulation outcomes for Case 8. (a1)–(a4) Active power output of various GFM-RPG units. (b1)–(b4) Angular frequency output of different GFM-RPG units.

VI. CONCLUSION

This study examines the transient stability criteria and control strategies for paralleled GFM-RPGs. The main findings are summarized as follows:

1) The damping term plays a crucial role in determining the transient stability of paralleled GFM-RPG systems. Neglecting its effect can lead to overly conservative analytical results. To improve this limitation, the study utilizes a numerical solution of a differential equation to explore the variation patterns of CCA and CCT in the paralleled system while incorporating the damping effect. The results indicate that increasing damping and fault impedance, as well as reducing the equivalent active power reference value, collectively contribute to improved transient stability of the system;

2) To improve the stable operation performance of paralleled GFM-RPG systems during symmetrical faults, this study proposes two advanced stabilization control strategies: adaptive damping enhancement and power switching. Both approaches effectively improve CCA and CCT, thereby mitigating the risk of transient instability.

The results of this study offer valuable insights and practical guidelines for assessing and improving transient stability in practical islanded microgrids under symmetrical faults.

APPENDIX A

TABLE AI
SIMULATION SYSTEM PARAMETERS FOR RPGS

Symbol	Description	Value
P_n MW (1 p.u.)	Rate power	2
V_n V (1 p.u.)	Rate voltage	690
V_{dc} (V)	DC-link voltage	1200
f_g (Hz)	Rate frequency	50
L_f (p.u.)	Filter inductance	0.25
C_f (p.u.)	Filter capacitor	0.15
Z_1/Z_2 (p.u.)	Line impedance	0.15+j0.55
Z_L (p.u.)	Load impedance	0.5870+0.3926
Z_F (p.u.)	Fault impedance	0.01
Z_V (p.u.)	Virtual impedance	0.05+j0.35
J_1/J_2	Virtual inertia	4.5/9.0
D_1/D_2	Virtual damping	18/36
P_{ref1}/P_{ref2}	Power reference value	1/0.5
K_{q1}/K_{q2}	Reactive power loop coefficient	0.001

TABLE AII
SYSTEM PARAMETERS OF THE TWO-AREA MODEL WITH FOUR-CONVERTER SYSTEM

Symbol	Description	Value
P_n MW (1 p.u.)	Rate power	100
V_n V (1 p.u.)	Rate voltage	690
V_{dc} (V)	DC-link voltage	1200
f_g (Hz)	Rate frequency	50
L_f (p.u.)	Filter inductance	0.13
C_f (p.u.)	Filter capacitor	0.075
R (p.u./km)	Line resistance	0.0081
X (p.u./km)	Line reactance	0.01
Z_F (p.u.)	Fault impedance	0.01
Z_V (p.u.)	Virtual impedance	0.01+j0.3
J	Virtual inertia	5
D	Virtual damping	25
K_q	Reactive power loop coefficient	0.01
l_6/l_7	Line	25 km/10 km
l_8/l_9	Line	110 km/10 km
l_{10}	Line	25 km

ACKNOWLEDGMENT

Not applicable.

AUTHORS' CONTRIBUTIONS

Sen Huang: theoretical derivation, simulation, and full-text writing. Jun Yao: writing review and editing, the full-text revise, and supervision. Wenwen He: data curation and formal analysis. Dong Yang and Hai Xie: simulation and full-text revision. All authors read and approved the final manuscript.

FUNDING

This work is supported by Joint Research Fund in Smart Grid (No. U1966208) under cooperative agreement between the National Natural Science Foundation of China and State Grid Corporation of China.

AVAILABILITY OF DATA AND MATERIALS

Not applicable.

DECLARATIONS

Competing interests: The authors declare that they have no known competing financial interests or personal relationships that could have appeared to influence the work reported in this article.

AUTHORS' INFORMATION

Sen Huang received the B.Eng. degree in electrical engineering and automation from Northwest A&F University, Xianyang, China, in 2019, and received the Ph.D. degree in electrical engineering from Chongqing University, Chongqing, China, in 2024. His research interests include power electronics conversion and control, modeling and control of renewable power generation.

Jun Yao received the B.Eng., M.S., and Ph.D. degrees in electrical engineering from Chongqing University, Chongqing, China, in 2001, 2004, and 2007, respectively. Since 2004, he has been with the School of Electrical Engineering, Chongqing University, where he is currently a professor. From January 2012 to January 2013, he was a visiting researcher at the Department of Energy Technology, Aalborg University, Aalborg, Denmark. He is the author or co-author of more than 100 peer-reviewed technical papers and holds more than 20 issued or pending patents. His research interests include electric machines control, power electronics conversion and control, renewable power generation, and wind energy and power electronics application to the power systems. He is a member of IEC TC 8/SC 8A/JWG 5.

Wenwen He received the B.Eng. degree in electrical engineering and automation from China University of Mining and Technology, Xuzhou, China, in 2021, and the M. Sc. degree in electrical engineering from the School of Electrical Engineering, Chongqing University, Chongqing, China, in 2024. His research interests include transient stability analysis and control of virtual synchronous generator.

Dong Yang received the B.Eng. degree in electrical engineering and automation from Yanshan University, Qinhuangdao, China, in 2022. He is currently working toward the Ph.D. degree with the School of Electrical Engineering, Chongqing University, Chongqing, China. His research interests include control of stability of power system and renewable power generation.

Hai Xie received the B.Eng. degree in electrical engineering and automation from Taiyuan University of Technology, Taiyuan, China, in 2022, and the M. Sc. degree in electrical engineering from the School of Electrical Engineering, Chongqing University, Chongqing, China, in 2025. His research interests include large-disturbance stability analysis of wind energy conversion system and grid-forming control.

REFERENCES

[1] X. Wang, M. G. Taul, and H. Wu *et al*., "Grid-synchronization stability of converter-based resources—an overview," *IEEE Open Journal of Industry Applications*, vol. 1, pp. 115-134, Aug. 2020.

[2] H. Yuan, H. Xin, and L. Huang *et al*., "Stability analysis and enhancement of type-4 wind turbines connected to very weak grids under severe voltage sags", *IEEE Transactions on Energy Conversion*, vol. 34, no. 2, pp. 838-848, Jun. 2019.

[3] J. Hu, Y. Huang, and D. Wang *et al*., "Modeling of grid-connected DFIG-based wind turbines for DC-link voltage stability analysis," *IEEE Transactions on Sustainable Energy*, vol. 6, no. 4, pp. 1325-1336, Oct. 2015.

[4] X. He, Q. Ai, and R. C *et al*., "A big data architecture design for smart grids based on random matrix theory, "*IEEE Transactions on Smart Grid*, vol. 8, no. 2, pp. 674-686, Mar. 2017.

[5] H. Wu and X. Wang, "Design-oriented transient stability analysis of PLL-synchronized voltage-source converters," *IEEE Transactions on Industrial Electronics*, vol. 35, no. 4, pp. 3573-3589, Apr. 2020.

[6] X. He, H. Geng, and R. Li *et al*., "Transient stability analysis and enhancement of renewable energy conversion system during LVRT, "*IEEE Transactions on Sustainable Energy*, vol. 11, no. 3, pp. 1612-1623, Jul. 2020.

[7] Y. Zhang, C. Zhang and X. Cai, "Large-signal grid-synchronization stability analysis of PLL-based VSCs using Lyapunov's direct method," *IEEE Transactions on Power Systems*, vol. 37, no. 1, pp. 788-791, Jan. 2022.

[8] Q. Zhong and G. Weiss, "Synchronverters: inverters that mimic synchronous generators," *IEEE Transactions on Industrial Electronics*, vol. 58, no. 4, pp. 1259-1267, Apr. 2011.

[9] Z. Shuai, C. Shen, and X. Liu *et al*., "Transient angle stability of virtual synchronous generators using Lyapunov's direct method," *IEEE Transactions on Smart Grid*, vol. 10, no. 4, pp. 4648-4661, Jul. 2019.

[10] H. Cheng, Z. Shuai, and C. Shen *et al*., "Transient angle stability of paralleled synchronous and virtual synchronous generators in islanded microgrids," *IEEE Transactions on Power Electronics*, vol. 35, no. 8, pp. 8751-8765, Aug. 2020.

[11] P. Ge, C. Tu, and F. Xiao, *et al*., "Design-oriented analysis and transient stability enhancement control for a virtual synchronous generator," *IEEE Transactions on Industrial Electronics*, vol. 70, no. 3, pp. 2675-2684, Mar. 2023.

[12] Z. Miao, "Impedance-model-based SSR analysis for type 3 wind generator and series-compensated network," *IEEE Transactions on Energy Conversion*, vol. 27, no. 4, pp. 984-991, Dec. 2012.

[13] Y. Liao, X. Wang, and F. Liu *et al*., "Sub-synchronous control interaction in grid-forming VSCs with droop control," in *2019 4th IEEE Workshop on the Electronic Grid (eGRID)*, Xiamen, China, Mar. 2019, pp. 1-6.

[14] W. Deng, W. Pei, and Q. Wu *et al*., "Analysis of interactive behavior and stability of low-voltage multiterminal DC system under droop control modes," *IEEE Transactions on Industrial Electronics*, vol. 69, no. 7, pp. 6948-6959, Jul. 2022.

[15] Y. Cheng, "Real-world subsynchronous oscillation events in power grids with high penetrations of inverter-based resources," *IEEE Transactions on Power Systems*, vol. 38, no. 1, pp. 316-330, Jan. 2023.

[16] A. Fathi, Q. Shafiee, and H. Bevrani, "Robust frequency control of microgrids using an extended virtual synchronous generator," *IEEE Transactions on Power Systems*, vol. 33, no. 6, pp. 6289-6297, Nov. 2018.

[17] P. Sun, J. Yao, and Y. Zhao *et al*., "Stability assessment and damping optimization control of multiple grid-connected virtual synchronous generators," *IEEE Transactions on Energy Conversion*, vol. 36, no. 4, pp. 3555-3567, Dec. 2021.

[18] H. Wu and X. Wang, "Design-oriented transient stability analysis of grid-connected converters with power synchronization control," *IEEE Transactions on Industrial Electronics*, vol. 66, no. 8, pp. 6473-6482, Aug. 2019.

[19] D. Pan, X. Wang, and F. Liu *et al*., "Transient stability of voltage-source converters with grid-forming control: a design-oriented study," *IEEE Journal of Emerging and Selected Topics in Power Electronics*, vol. 8, no. 2, pp. 1019-1033, Jun. 2020.

[20] S. Chen, Y. Sun, and X. Hou *et al*., "Quantitative parameters design of VSG oriented to transient synchronization stability," *IEEE Transactions on Power Systems*, vol. 38, no. 5, pp. 4978-4981, Sept. 2023.

[21] J. Lei, X. Xiang, and B. Liu *et al*., "Quantitative and intuitive VSG transient analysis with the concept of damping area approximation," *IEEE Transactions on Smart Grid*, vol. 14, no. 3, pp. 2477-2480, May 2023.

[22] J. Lei, X. Xiang, and B. Liu *et al*., "Transient stability analysis of grid forming converters based on damping energy visualization and geometry approximation," *IEEE Transactions on Industrial Electronics*, vol. 71, no. 3, pp. 2510-2521, March 2024.

[23] G. Wang, L. Fu, and Q. Hu *et al*., "Transient synchronization stability of grid-forming converter during grid fault considering transient switched operation mode," *IEEE Transactions on Sustainable Energy*, vol. 14, no. 3, pp. 1504-1515, Jul. 2023.

[24] H. Xin, L. Huang, and L. Zhang *et al*., "Synchronous instability mechanism of P-f droop-controlled voltage source converter caused by current saturation," *IEEE Transactions on Power Systems*, vol. 31, no. 6, pp. 5206-5207, Nov. 2016.

[25] X. Xiong, C. Wu, and F. Blaabjerg, "Effects of virtual resistance on transient stability of virtual synchronous generators under grid voltage sag," *IEEE Transactions on Industrial Electronics*, vol. 69, no. 5, pp. 4754-4764, May 2022.

[26] H. Wu and X. Wang, "A mode-adaptive power-angle control method for transient stability enhancement of virtual synchronous generators," *IEEE Journal of Emerging and Selected Topics in Power Electronics*, vol. 8, no. 2, pp. 1034-1049, June 2020.

[27] X. Xiong, C. Wu, and P. Cheng *et al*., "An optimal damping design of virtual synchronous generators for transient stability enhancement," *IEEE Transactions on Power Electronics*, vol. 36, no. 10, pp. 11026-11030, Oct. 2021.

[28] X. Xiong, C. Wu, and B. Hu *et al*.,"Transient damping method for improving the synchronization stability of virtual synchronous generators," *IEEE Transactions on Power Electronics*, vol. 36, no. 7, pp. 7820-7831, Jul. 2021.